earth

MDPI

Article

Interannual Variability of Ephemeral Snow and Its Water Equivalent in a Mexican Mediterranean Mountain Region

Mariana E. Espinosa-Blas [1], Trent W. Biggs [2], Alejandro González-Ortega [3], Gorgonio Ruiz-Campos [4], Leopoldo G. Mendoza-Espinosa [1] and Napoleon Gudino-Elizondo [1,*]

[1] Instituto de Investigaciones Oceanológicas, Universidad Autónoma de Baja California, Carretera Ensenada-Tijuana No. 3917, Fracc. Playitas, Ensenada 22860, Mexico; elizabeth.espinosa@uabc.edu.mx (M.E.E.-B.); lmendoza@uabc.edu.mx (L.G.M.-E.)
[2] Department of Geography, San Diego State University, San Diego, CA 92182, USA; tbiggs@sdsu.edu
[3] División de Ciencias de la Tierra, Centro de Investigación Científica y de Educación Superior de Ensenada, Carretera Ensenada-Tijuana No. Zona Playitas, Ensenada 22860, Mexico; aglez@cicese.mx
[4] Facultad de Ciencias, Universidad Autónoma de Baja California, Carretera Transpeninsular 3917, Fraccionamiento Playitas, Ensenada 22860, Mexico; gruiz@uabc.edu.mx
* Correspondence: ngudino@uabc.edu.mx

Abstract

Increasing temperature and decreasing precipitation threaten the extent, persistence, and dynamics of snow across spatial scales, particularly ephemeral snow in Mediterranean mountain regions. This study estimates ephemeral snow cover and snow water equivalent (SWE) in the Sierra de San Pedro Mártir, Baja California, Mexico, using open-access datasets and remote sensing. Camera trap images and limited in situ data were used to calibrate the normalized difference snow index (NDSI) for snow detection and to estimate SWE and topographic effects on SWE from 2002 to 2023, encompassing wet, dry, and normal years. The optimal NDSI threshold for snow detection was 6.4 for MODIS Terra and 5.3 for MODIS Aqua, substantially lower than thresholds commonly reported for seasonal snowpacks in forested regions. In wet years, snowfall contributed up to 20% of annual precipitation, compared with ~13% in dry years. In normal years, the average SWE is 70 mm (24% of annual precipitation). SWE increased by 30% (91 mm) during wet years and decreased by 21% (55 mm) during dry years. Eastness (aspect) was the only statistically significant topographic predictor of SWE for MTerra, with higher SWE values observed on west-facing slopes. This study provides the first quantitative assessment of ephemeral SWE dynamics in a Mexican Mediterranean mountain system and establishes a framework for monitoring marginal snowpacks under increasing climatic variability.

Keywords: ephemeral snow; Mediterranean mountain; snow water equivalent; remote sensing; NDSI; MODIS; GEE

Academic Editor: Steven R. Fassnacht

Received: 16 January 2026
Revised: 27 February 2026
Accepted: 28 February 2026
Published: 4 March 2026

1. Introduction

Snow cover and its water content are decreasing in mountain areas worldwide due to climate change [1]. The snowline is expected to migrate to higher elevations, leading to reduced snow accumulation [2] and shorter snowpack duration [3]. The reduction in snow cover will impact watershed hydrology by increasing evapotranspiration and reducing groundwater recharge, while also affecting socio-ecological processes by decreasing water supplies and increasing risks of flooding and wildfires [4,5]. However, the magnitude of climate change impacts on snow remains uncertain in regions dominated by ephemeral and transitional snow regimes across different climates and spatial scales [5].

Recent studies have introduced the concept of marginal snowpack to describe transitional snow regimes characterized by intermittent accumulation, limited persistence, and high sensitivity to temperature variability [6,7]. Marginal snowpacks occupy a continuum between seasonal and ephemeral snow classes and are particularly common in Mediterranean mountain environments, where strong inter- and intra-annual climatic variability leads to pronounced spatial and temporal heterogeneity in snowpack depth, duration, and extent [6–9]. This variability is especially evident in areas dominated by short-lived and shallow snow events. Ephemeral snow (ES) cover is defined as snow cover resulting from individual storm events. Depending on the environmental conditions, ephemeral snow can persist from a few hours to several weeks, typically with shallow snow depths [3,8]. The dynamics of ES—including snowfall, interception, sublimation, and melt—are influenced by vegetation structure and density [10] as well as local climatic and topographic conditions such as elevation, aspect, and slope. These factors influence snowpack duration and its water content, commonly expressed as snow water equivalent (SWE).

The hydrological role of ephemeral snow remains poorly understood. In Mediterranean mountain regions, ES melt contributes up to approximately 30% of winter runoff [11]. In dense forests, up to 50% of snowfall may reach the soil, enhancing infiltration and generating multiple soil moisture pulses during winter [12]. In landscapes characterized by low tree density and heterogeneous forest structure across landforms such as canyons, slopes, and ridges [13], significant knowledge gaps persist regarding the contribution of snow cover area (SCA) and SWE to watershed hydrology and the implications of snowpack decline under climate warming [10,12].

Previous studies highlight the need for improved characterization of ephemeral snow dynamics across climate gradients and ecohydrological contexts [3,12,14]. Remote sensing approaches have been widely applied to overcome limitations associated with sparse in situ observations. Snow cover area is commonly estimated using the normalized difference snow index (NDSI), which uses the green and shortwave near-infrared (SWIR) bands, with a conventional threshold of 0.4 to indicate snow presence [15]. However, this threshold is not universally applicable, as it depends on vegetation cover, snow depth, and topographic conditions [16–18]. Camera traps provide valuable ground-based observations that can support the calibration of NDSI thresholds, improve snow detection in remote areas, and document snow dynamics [10,12,19,20].

In addition to SCA, SWE is a primary measure of snow variability in mountain regions. SWE reconstruction based on a time series of SCA and a mass ablation balance model has been applied to overcome the challenges of field measurements with accurate results even in areas with scarce reference data [21–24].

This study analyzes the interannual variability of the snow cover and snow water equivalent of ephemeral snow and its topographic controls in the coniferous forest of the supra-Mediterranean belt (>2000 m.a.s.l.) in the Sierra de San Pedro Mártir (SSPM), Baja California, Mexico, to address three primary research questions: (1) How sensitive is MODIS V6 to detect ephemeral snow cover area (SCA) in low-density forests and open vegetation between Terra and Aqua MODIS observations? (2) Are there temporal trends in SCA and SWE over time? (3) What environmental conditions control the spatial and temporal differences in SCA and SWE over two decades? We hypothesized that (a) defining an optimal threshold for snow detection in the SSPM improves the estimation of SCA and SWE across a region with sparse vegetation and steep topography, and (b) there is a difference between the values of SCA estimated from Terra and Aqua due to the short duration of the snowpack and to differences in the time of overpass.

To answer these questions, we identify an optimal NDSI threshold for snow detection and quantify the dynamics of ephemeral SCA and SWE and their evolution through the

reconstruction of 20 years of SWE in the study area. This information improves strategies for adapting to climate change and water resource management to conserve ecosystems and the hydrologic services of the SSPM that provide benefits to downstream communities and ecosystems.

2. Materials and Methods

2.1. Study Area

The SSPM is located in the north central portion of the state of Baja California, Mexico (Figure 1). The zone has a Mediterranean climate, with an average air temperature of 10.3 °C during the day and 7 °C at night. Precipitation occurs primarily during winter frontal systems and summer convective storms associated with the North American Monsoon [25,26], resulting in a bimodal precipitation regime that reflects a Mediterranean climate modified by monsoonal influence. The average annual rainfall ranges from 260 mm at low elevations to 700 mm at high elevations [27]. In winter, 50% of the precipitation falls as snow [27], which is considered an important source of moisture to the ecosystems [28], which include approximately 500 vascular plant species [29], 27 herpetofauna species [30], 54 mammalian species [31], 193 bird species [32], and 2 fishes species [33], with a high percentage of endemic species.

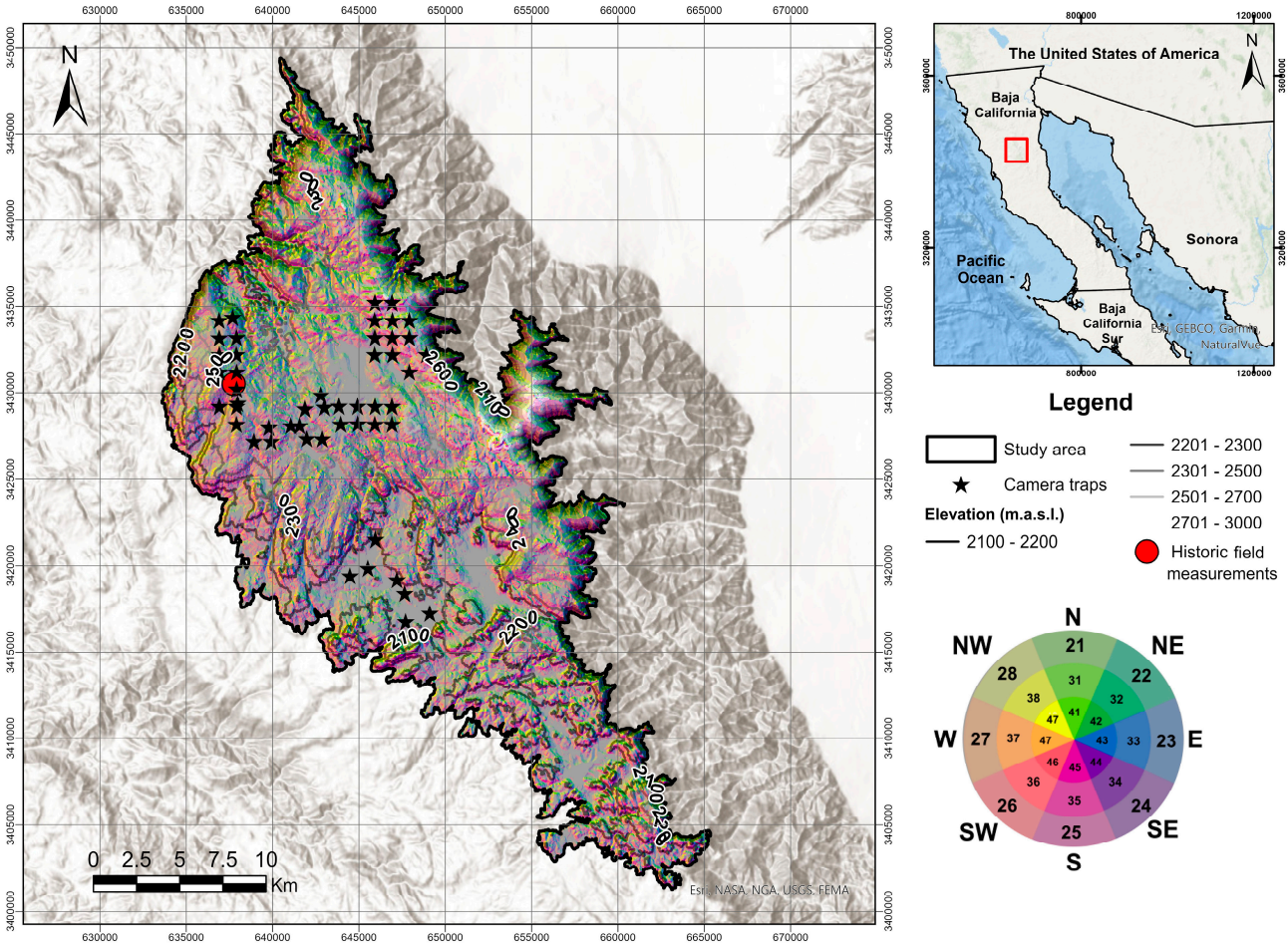

Figure 1. The Sierra de San Pedro Mártir (SSPM) study area (black line). The elevation of the SSPM is represented on a color scale from black to white at the highest elevations. The Aspect-Slope Map of the forest delimitation in the SSPM is on a color scale (from yellow to magenta). Camera traps are indicated by black stars and the historic point field measurement in a red dot. Red polygon indicates the regional location of the study area.

In the SSPM, there are three main types of vegetation whose ranges are influenced by elevation: coniferous forest (high-elevation), chaparral (mid-elevation), and shrubs (low-elevation) [28,34]. The mixed coniferous forest is an open forest with low tree density and mature trees [27], representing one of the main forest reserves in the state [35], which since 1947 has been declared a Protected Natural Area (PNA) as a National Park [35].

The main ecosystem services in the SSPM include the hydrological service of recharging the coastal aquifers that supply water resources to the population of the San Quintin Valley and nearby towns [36]. There is a knowledge gap of how communities depend on these ecosystem services, mainly because the lack of knowledge of how much water the Sierra produces [36] and the impacts or contribution of snow in different socioecological systems in the Sierra and its surroundings.

2.2. Ephemeral Snow Mapping

Mapping SCA, SWE, and their topographic controls was carried out using remote sensing techniques and workflows developed through the Google Earth Engine (GEE) platform. GEE is a cloud platform for processing, analysis, and management of big data from Earth observations (satellite images or reanalysis data) [37]. Two main scripts were developed, one to generate an SCA time series and one to homogenize the projection and the spatial resolution between the environmental variables for the reconstruction of the SWE (Table 1). To account for elevation-dependent temperature variability during downscaling from ERA5-Land (11 km) to the MODIS 500 m grid, a standard environmental lapse rate of $-6.5\ ^{\circ}C\ km^{-1}$ was applied [38].

Table 1. Variables selected in GEE to reconstruct SWE.

Variable	Dataset	Units	Spatial Resolution	Temporal Resolution
Temperature	ERA5 land—hourly	K → °C	11 km *	daily/h 1981–present
Precipitation		m/h → mm/day		
Net radiation		W/m^2		
Snow density		kg/m^3		
NDSI [1]	Modis collectionV6: Terra (MOD10A1) and Aqua (MYD10A1)	Dimensionless	500 m	daily 2002–2023

* Downscaling to MODIS resolution; [1] Estimation of SCA through the NDSI.

Pixel-wise fractional SCA (0–1) was mapped using the MODIS (Moderate-Resolution Imaging Spectroradiometer) for Terra (MTerra), the MOD10A1 collection, and for Aqua (MAqua) MYD10A1 of the snow products, which have a daily global resolution of 500 m with a difference of observations between orbital passes of 3 h (MTerra 10:30, MAqua 13:30) [15].

We generated a time series of SCA for 20 water years (2003–2023) from Terra and Aqua satellites in the winter season and compared them with camera traps to define an optimal normalized difference snow index (NDSI) threshold for ES in the SSPM.

2.2.1. SCA: Ground Reference, NDSI Thresholds, and Validation

To select the optimal threshold of the NDSI for the SSPM, a confusion matrix (Appendix A.1: Table A1) was built using the winter season images from camera traps (n = 87 images) deployed within the National Park in the SSPM to provide a ground reference of snow presence at different time periods: 2011–2013, 2015–2016, and 2022–2023 (Appendix A.1: Figure A1). The trap images closest to the MODIS pass times (10:30 and

13:30) were selected for validation (49 for MTerra and 38 for MAqua). The NDSI at the location of the camera traps was compared with the NDVI ($\leq$0.1) to corroborate snow cover in pixels with uncertainty (according to the NDSI snow cover class bands from MODIS (V6) about the snow presence [39]). The images from camera traps were classified visually into four classes (0–25%, 50%, 75%, and 100% snow cover).

Local optimal thresholds of NDSI were determined by varying NDSI thresholds from 0 to 100 and creating binary SCA maps for each threshold. The accuracy of each map was quantified using the ROC (Receiver-Operating-Characteristic) analysis following [19]. We developed the workflow in RStudio 4.3.3 [40] using the pROC package [41]. The ROC curve is a statistical analysis used to evaluate the relationship between the sensitivity (true positive rate) as a function of false positive rate (1 − specificity) in different cut-off points or thresholds [41]. The optimal NDSI threshold was defined with the Youden Index (sensitivity + specificity −1), which represents the cut point of the maximum sensitivity and SP metrics [42]. In this case, the NDSI threshold is reported on a scale of 0–100, according to the scale used in the dataset of MODIS V6. In previous studies, NDSI values were commonly reported between −1 and 1. In MODIS Collection 6, however, the NDSI is rescaled to a 0–100 range [19].

The performance of the binary classification was assessed using the following metrics: overall accuracy (OA), precision (P), specificity (SP), and sensitivity (S) (Appendix A.1: Equations (A1)–(A4)).

2.2.2. SWE Reconstruction

The optimal NDSI threshold for each satellite was used to map SCA and to select days with snowfall events, defined as days with precipitation greater than zero but temperature lower than the temperature threshold for snow ($\leq$4 °C) [43] from the ERA5-Land dataset. The SWE was reconstructed using the melt potential model (Table 2) for each pixel's snow cover depletion cover [21] for each snowfall event in the SSPM.

Table 2. Description of the variables used in the model of SWE reconstruction.

Reference	Description of Variables	Equation	No.
[21]	Mp_j: melting potential (mm/day) Td_j: mean daily air temperature (>0°). Rn_j: daily net radiation (w/m^2). *DDF*: the degree day factor (cm °C^{-1} day^{-1}) Mq_j: the energy of water depth conversion (0.026 cm W^{-1} m^{-2} day^{-1}) J: day of analysis	$Mp_j = Td_j$ x DDF + Rn_j x Mq_j	(1)
[44]	ρw: density of water ρs: density of snow	$DDF = 1.1\left(\frac{\rho s}{\rho w}\right)$	(2)
[21]	M_j = melt potential generated by the energy exchange of the SCA SCA_j = the fractional snow cover area	$M_j = Mp_j$ x SCA_j	(3)
[15]	NDSI = values of NDSI (MTerra or MAqua)	$SCA_j = -0.01 + 1.45$ x NDSI	(4)
[21]	SWE: sum of the of the potential snowmelt for each snowfall event	$SWE = \sum_{j=1} Mpj,$	(5)

We also compared SWE estimates from each satellite and assessed their diurnal differences by computing the mean of the MTerra and MAqua SWE estimates (hereafter referred to as SWE match).

2.3. Variation of SWE Reconstruction Between Climate Conditions

For the 20 water years of analysis, we identify wet, dry, and normal water years using the Standardized Precipitation Evapotranspiration Index (SPEI), which is an indicator of drought season in multiple years. The SPEI is the difference between precipitation and the potential evapotranspiration to determine when a year is wet (>0.5), normal (−0.5 to 0.5), or dry (<−0.5) [45,46]. These wet–dry periods were used to compare the SWE estimation in ephemeral conditions in a Mediterranean climate and identify the years that could act as a proxy for the possible effects of climate change in terms of snowmelt accumulation.

2.4. Cross-Validation of the SWE Reconstruction and Topographic Controls

Validation of the SWE reconstruction was carried out using in situ SWE measurements taken in the SSPM National Park from December 2021 to March 2023 and K-fold cross-validation. The K-fold method divides the dataset into equal subsets to generate a testing and training dataset k times for validation [47]. The literature recommends using 5 or 10 k-folds, depending on the database and the computational resources [48]. We used 5 k-folds in the cross-validation. At the end, four metrics were calculated: R2 (determination coefficient), RMSE (root mean square error), NRMSE (RMSE divided by the mean observed SWE, resulting in a unitless metric), and the bias (prediction—observation).

2.5. Relationship Between Topographic Variables

Topographic variables (elevation, slope, and aspect) were estimated using a DEM (Digital Elevation Model) from INEGI (National Institute of Statistics and Geography) with a spatial resolution of 15 m (Figure 1). The aspect was transformed to a continuous gradient as Northness and Eastness followed Equations (6) and (7). The values range between −1 and 1, where values near 1 indicate an aspect to the north (Northness) or east (Eastness).

$$\text{Northness} = \cos(\text{aspect}) * \sin(\text{slope}) \quad (6)$$

$$\text{Eastness} = \sin(\text{aspect}) * \sin(\text{slope}) \quad (7)$$

Multiple regression modeling was performed in RStudio to test the hypothesized relationship between topographic variables and SWE. Statistical significance of regression coefficients was assessed using *t*-tests (*p*-values). We hypothesized that higher SWE values would occur on north-facing slopes and at higher elevations due to lower temperatures and reduced solar radiation and on gentler slopes where snow redistribution is minimized. Although vegetation strongly influences SWE in many mountain systems, forest density in the SSPM is relatively low and spatially homogeneous compared to dense conifer forests in temperate regions. Therefore, vegetation effects were not explicitly included in the regression model but should be considered in future studies incorporating canopy structure data.

3. Results

3.1. SCA Observations and the Optimal Threshold of NDSI

The NDSI-based snow presence and observed snow presence from camera traps had 81% overall accuracy for each satellite. The other assessment metrics differed between the two satellites. For MTerra, both precision and specificity were 100%. For MAqua observations, the precision was 89%, and the specificity was 96%, since at least one false positive was found in the validation. The sensitivity was 52% and 57% for MTerra and MAqua, respectively (Table 3), indicating that a little more than half of the images with snow from the camera traps also had MODIS-indicated snow.

Table 3. Classification performance metrics for MTerra and MAqua.

Observed Class	MTerra		MAqua	
	Snow	**No Snow**	**Snow**	**No Snow**
Snow	10	9	8	6
No snow	0	30	1	23
OA (%)	82		82	
P (%)	100		89	
SP (%)	100		96	
Sensitivity (%)	52		57	
ROC-AUC	0.75		0.76	
ROC-Optimal threshold	6.43		5.35	

The optimal NDSI threshold in the SSPM was 6.43 for MTerra and 5.35 for MAqua. These values had an area under the curve (AUC) of 0.75 (MTerra) and 0.76 (MAqua); this means that for these NDSI thresholds, the probability of the model distinguishing between the snow and no snow classes is 75% and 76% using MTerra and MAqua, respectively (Table 3).

3.2. Interannual Variability of Ephemeral Snow and Its Water Equivalent

In the 20-year analysis of climatic variables (2003–2023), in the forest zone, the mean annual precipitation from ERA-5 LAND was 300 mm, the mean minimum temperature was 9 °C, and the maximum was 20 °C; in the winter, the mean precipitation was 111 mm, the temperature was 8 °C, and the SCA percentage was around 25% per pixel (the highest SCA was 73), which is equivalent to up to 180 mm depending on the climatic conditions.

Based on SPEI, the wettest water years (WWY) were 2005, 2010, 2015, 2019, and 2023, while the driest water years (DWY) were 2003, 2007, 2011, 2012, 2018, 2021, and 2022. The remaining years were classified as near-normal (NWY): 2004, 2006, 2008, 2009, 2013, 2014, 2016, 2017, and 2020.

Precipitation during the 20-year period exhibited clear seasonal partitioning between summer and winter rainfall. In wet years, winter precipitation accounted for approximately 47% of the annual total, compared to 28% in dry years and 35% in normal years. The contribution of SWE varied with climatic conditions; on average, across all years, snowfall represented approximately 65% of winter precipitation (Figure 2). This corresponds to approximately 12–20% of total annual precipitation depending on water year type.

Using the NDSI threshold, we identified 193 snowfall events, whose cumulative SWE represents 18% of total precipitation, including 154 events identified with MTerra and 164 with MAqua. The years with the most events were 2010 and 2023 (14 events), and the month with the most snowfall was February for both satellites (6 events in 2010 and 2023, both considered as WWY).

The maximum total SWE occurred in the 2010 water year, with 192 mm and 122 mm accumulated in MTerra and MAqua, respectively. The water years with the minimum total SWE (non-zero) were 2018 (14 mm in MTerra) and 2015 (18 mm in MAqua). The event with the maximum SWE was March 2020 for MTerra (76 mm) and February 2023 for MAqua (62 mm). In the case of the potential SWEmatch (average of MTerra and MAqua estimations), the maximum SWE was February (59 mm in 2009), and the minimum non-zero SWE occurred in December 2021 (4 mm, Figure 3c).

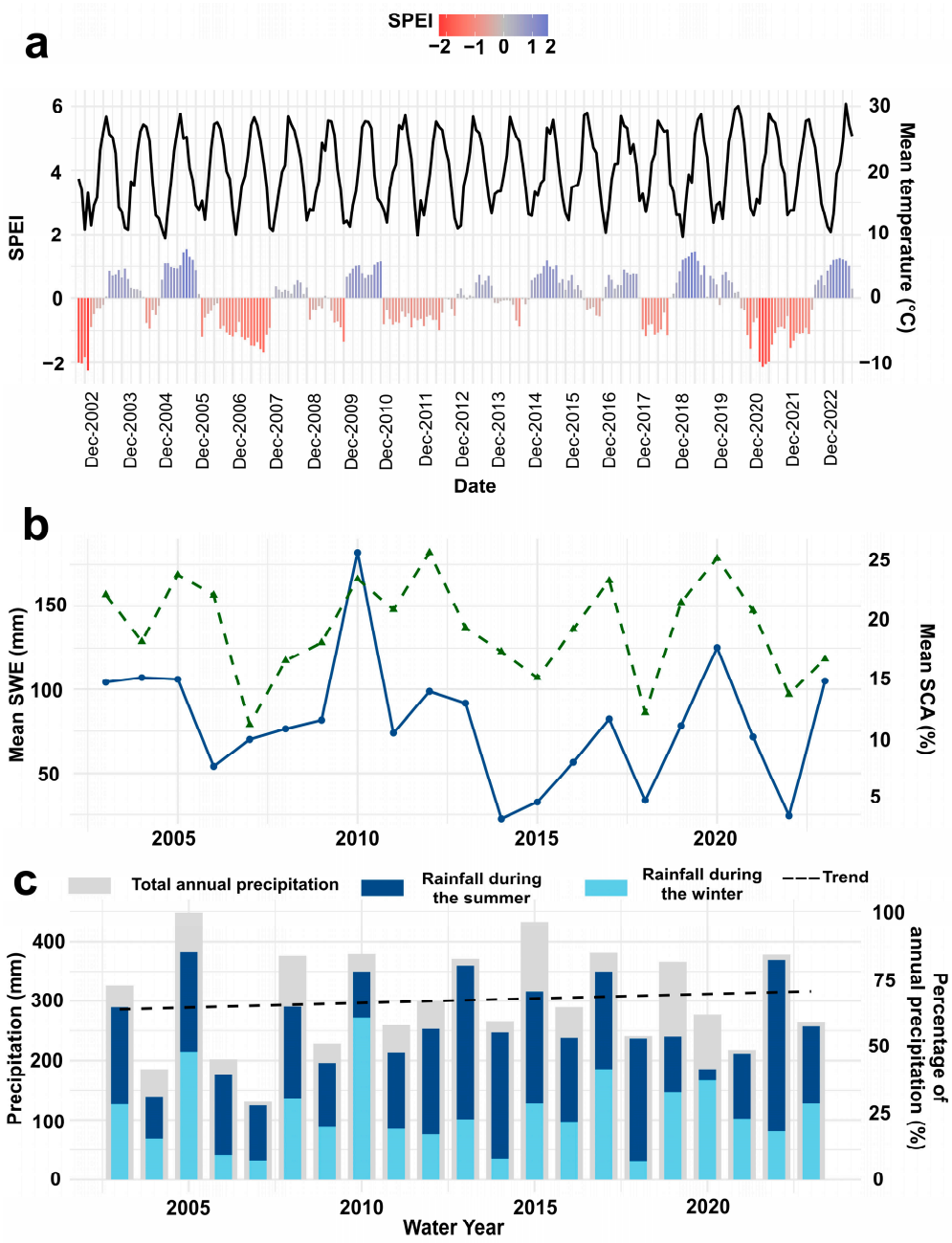

Figure 2. Comparison of the time series (2003–2023) of the SPEI (color scale from red (DWY) to blue (WWY) and mean air temperature (black solid line) in the SSPM (**a**). The mean SCA (dotted green line) compared with mean SWE results (blue solid line) (**b**) and the proportion of rainfall for the summer season (blue bar) and winter (light blue bar) per water year from the total annual precipitation (gray bar) and its trend (dotted black line) (**c**).

There were statistically significant differences in SWE between WWY and DWY for both satellites, according to the Wilcoxon test (W = 15797, and $p < 0.001$). In dry years, there was a difference of up to 35% between the two satellite estimations of SWE, while in wet years, the difference was 12%, compared to 33% in normal years. The mean SWE in WWYs was 21 mm higher (30%) than in NWY (mean = 70 mm), while in dry conditions, a deficit of 15 mm (21%) is expected (Appendix A.2: Figure A2).

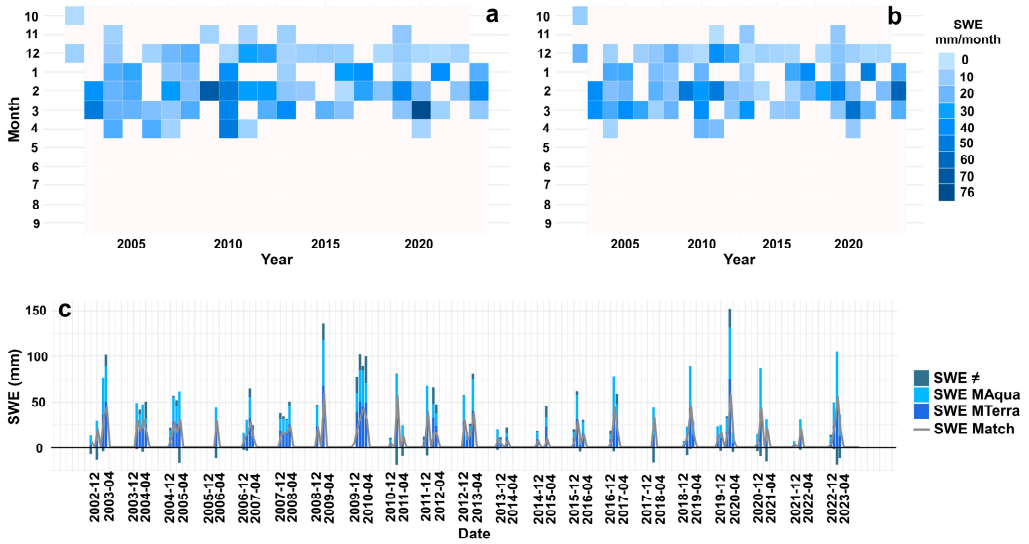

Figure 3. Interannual variability of SWE (mm) reconstruction of the forest zone in the SSPM using MTerra (**a**) and MAqua (**b**) observations (scale color from light blue to dark blue), (**c**) the difference (sky blue bar) between SWE results from MTerra (blue bar) and MAqua (light blue bar), and the potential SWE by combining the SCA of both satellites (gray line).

3.3. Cross-Validation of SWE Reconstruction

SWE estimated by MAqua explains 62% of the variability in observed SWE, with an RMSE of 0.54 mm and an NRMSE of 0.27 (Table 3). In the case of SWE by MTerra, the RMSE was 0.66 mm, the NRMSE was 0.33, and the R^2 was 90%. Although MAqua presented lower RMSE, MTerra explained a higher proportion of variance (R^2). The potential SWE using both satellites (SWE match) for the 20 years of analysis results in an RMSE of 0.76 mm and NRMSE of 0.37, with 88% of SWE variability explained by the model. These results suggest that MTerra-derived SWE aligns more closely with in situ observations, possibly due to the timing of field measurements conducted in the morning corresponding more closely with Terra's overpass time (10:30–11:30) compared to Aqua (1:30–2:30 p.m.).

A positive bias of 0.05 mm was found with the SWE from MAqua, but using MTerra or using both satellites together (SWE match), the SWE was slightly underestimated (biases of −0.06 and −0.02 mm, respectively) (Table 4).

Table 4. Results of k-fold cross-validation of the SWE reconstruction and in situ dataset in the National Park (NP).

	NP In Situ Measurement (37 Samples)			
	R^2	**Bias (mm)**	**RMSE (mm)**	**NRMSE**
SWE MTerra	0.90	−0.06	0.66	0.33
SWE MAqua	0.62	0.05	0.54	0.27
SWEmatch	0.88	−0.02	0.76	0.37

3.4. Relationship Between SWE and Topographic Variables

In the forest, 84% of the total surface has slopes $\leq 30°$, and the exposure is preferentially oriented to the southwest, and 4% of the area is flat (slope < 1°). The aspect with higher SWE is to the west and south (Figure 4a,d). The highest SWE values are mostly located on slopes < 10° in both satellites (Figure 4b,e).

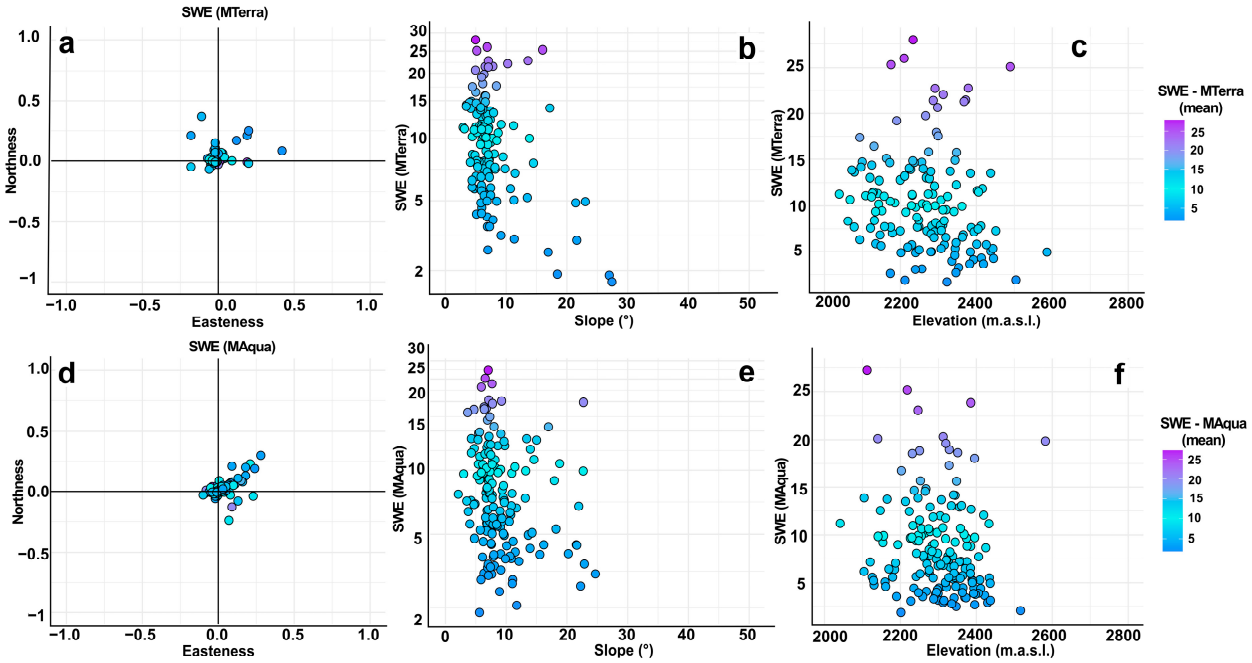

Figure 4. Topographic variables compared with the SWE reconstruction values in the forest zone. SWE MTerra comparatives are in (**a**) aspect (Northness–Eastness), (**b**) slope (°), and (**c**) elevation (m.a.s.l.); in the bottom panel are the MAqua estimations (**d**) aspect (Northness–Eastness), (**e**) slope (°), and (**f**) elevation (m.a.s.l.).

The forest elevation is between 2000 and 3098 m.a.s.l., and the elevations with relatively high SWE from both MTerra and MAqua range between 2000 and 2600 m.a.s.l. (Figure 4c,f). In MTerra, the highest value of SWE is at 2233 m.a.s.l. oriented SW and a slope of 5°, and the lowest non-zero value (1 mm) is at an altitude of 2322 m.a.s.l., oriented NE on a slope of 27°; for MAqua values, the highest value (27 mm) is at 2112 m.a.s.l., oriented to NW, on a slope of 7°, and the lowest values (2 mm) are at 2516 m.a.s.l., oriented to SW, on a slope of 12°. Spatially, SWE tended to occur on gentle slopes and on west- to south-facing aspects (Figure 4). However, in the multiple regression analysis (Table 5), Eastness was the only statistically significant predictor for MTerra ($p < 0.001$), whereas elevation, slope, and Northness were not significant. For MAqua, none of the analyzed topographic variables were statistically significant.

Table 5. Coefficients of the multiple regression analysis between SWE values (MTerra and MAqua) and the topographic variables (elevation, slope, and aspect).

	SWE MTerra				**SWE MAqua**			
	Estimate	**Std. Error**	**t Value**	***p*-Value**	**Estimate**	**Std. Error**	**t Value**	***p*-Value**
(Intercept)	5.18	3.31	1.56	0.120	2.46	0.55	4.41	1.86×10^{-5}
Elevation	−0.04	0.06	−0.67	0.50	−0.01	0.01	−1.01	0.31
Slope	0.94	1.66	0.56	0.57	1.20	0.86	1.39	0.16
Northness	0.98	1.13	0.86	0.38	−0.32	0.96	−0.33	0.73
Eastness	−5.72	1.42	−4.01	9.61×10^{-5}	−1.85	1.00	−1.84	0.06

In the multiple regression analysis (Table 5), Eastness was significantly related to SWE derived from MTerra ($p < 0.001$), with SWE decreasing by 5.72 mm (±1.42 mm) per unit increase in Eastness. In contrast, the other topographic variables were not statistically significant in MTerra observations. For MAqua, no significant relationship was found

between SWE and the analyzed topographic variables. Overall, these results suggest that the aspect was the dominant topographic control on SWE in the SSPM, particularly for MTerra observations, while future studies should explore additional environmental variables to better explain SWE variability derived from MAqua.

4. Discussion

We used the daily snow products of MODIS V6 to analyze the interannual variability of the SWE in the SSPM. Diverse studies have explored different methodologies to improve the SCA and SWE estimation on a global scale [49,50] and local scale [24,51], but there is a gap of information about the impacts and snow dynamics in low tree density with ephemeral snow.

4.1. SCA Observations

Estimates of SCA had an 81% overall accuracy compared with camera traps for both satellites, but sensitivity was only around 52–57% to identify the presence of snow in both datasets. The sensitivity values are significantly lower than those reported by Breen et al. [19] in Scandinavia using camera traps and MODIS, who found a true positive rate (sensitivity) of 88% using MTerra. One of the main reasons why the results are significantly different from previous work is the number of cameras and images used for the confusion matrix; in [19], hundreds of images were available from thousands of camera traps distributed in their study area. In our case, fewer cameras and images (n = 87 images) were available, and the cameras in the SSPM were preferentially located in the northern part of the park. It was not possible to capture snow cover at many different elevations and vegetation coverage. This suggests the need to expand the network of camera traps or equipment for snow monitoring to gather more precise information about the snow dynamics and impacts on ecosystems in the SSPM.

For the evaluation of accuracy between NDSI and absence/presence on the trap images, we had fewer than 50 images from five winter seasons because we chose the trap images closest to the time of satellite pass (MTerra and MAqua). The limited number of images could influence the evaluation and the complexity of estimating the SCA in ephemeral sites due to the shallow depth and heterogeneous distribution, as reported in other studies [52,53]. In future studies in the SSPM, it will be necessary to carry out field campaigns to estimate the snow depth, expand the network of camera traps, and propose other techniques to estimate diverse snow metrics and dynamics on Mediterranean mountains with ephemeral snow.

4.2. Optimal Threshold of NDSI

The optimal threshold of NDSI for the SSPM are 6.4 (MTerra) and 5.3 (MAqua), which were below the thresholds reported in recent studies (10 to 41), as well as the AUC results of 75% (MTerra) and 76% (MAqua). The optimal threshold of NDSI with MODIS observations is sensitive to the depth of the snowpack, vegetation, and topographic characteristics [17,18,54] and the altitude, snow depth, and latitude influence accuracy. The authors of [18,19] found an agreement between the SCA products by MODIS (MTerra) and the absence or presence of snow in images taken using camera traps and found an optimal threshold of 40.51 in a closed forest and an optimal threshold of 41.5 in open areas, results similar to the globally reported NDSI threshold reported by [55]. Our threshold NDSI values (5–6) are much lower, probably due to the patchy nature of snow cover.

In China, a threshold of 10 is reported to be optimal for better accuracy [18], but the threshold differs for each region, depth of snowpack, and vegetation. For example, using MODIS V6, the optimal threshold of NDSI was 0.2 for forests in Morocco [16] and for

thin snowpacks (<5 cm) in Italy [54]. In the results of our study and previous studies, differences are observed between the optimal threshold of NDSI and the accuracy obtained with MTerra and MAqua observations. According to [17], these differences are mostly in zones with irregular snow conditions and shallow depths (1–5 cm). Our results establish an important additional threshold of NDSI for ephemeral snowpacks.

In general, SWE depends on temperature and storm conditions [23]. In the SWE reconstruction, the maximum SCA and SWE are in WWY and the minimum in DWY. The mean percent difference between SCA or SWE from the MTerra and MAqua was 12% in WWY and higher (35%) in DWY, likely because dry years include patchier snow cover. Dry years may serve as analog conditions for potential warming-induced reductions in SWE because of the increase in temperature, which accelerated the melting process. Increased future temperatures would result in a decreased frequency of snowfall events, early melting, which means earlier pulses of soil moisture but, potential water stress in vegetation by the spring and summer. Continued research is needed to better understand the implications of changing snow regimes for downstream water availability and ecosystem services that support local communities.

In the study region (SSPM), snowfall only occurs in the winter and represents between 13% (DWY) and 22% (WWY) of annual precipitation, which is similar to other studies in Mediterranean mountains, including [11], where the melt of ephemeral snow contributes an average of 30% to annual discharge. Although dense forest cover typically reduces SWE due to canopy interception, the relatively open conifer forest in the SSPM may promote heterogeneous accumulation patterns, with localized retention due to shading depending on slope and aspect [52].

The SWE reconstruction based on a mass ablation balance model typically has high precision even in areas with scarce data and large basins [21–24]. According to the cross-validation, the SWE estimate using MAqua had a better fit (RMSE = 0.54 mm and NRMSE = 0.27) than SWE from MTerra (RMSE = 0.66 mm and NRMSE = 0.33) and from SWEmatch (RMSE = 0.76 mm and NRMSE = 0.37). In general, the SWE response depends on temperature and the timing of the storms [23], which was observed in the wet and dry periods, as well as in the results between MODIS observations. Differences between MTerra and MAqua estimates likely reflect diurnal melt processes, as Aqua overpasses occur approximately three hours later than Terra, potentially capturing additional snowmelt during sunny days.

The accuracy of SWE reconstruction models depends on the quality and spatial representativeness of temperature and radiation inputs [24]. Accounting for elevation-dependent temperature variability during ERA5-Land downscaling enhances the physical realism of the SWE reconstruction in this complex topographic setting, where ephemeral snow processes are highly sensitive to small thermal gradients [38]. We used MODIS and ERA5-Land as input datasets for SWE reconstruction; MODIS has demonstrated high reliability for snow cover mapping even in forested areas [56], and ERA5-Land (11 km spatial resolution) has shown strong performance for interannual variability analyses and for assessing trends and correlations of snow cover in regions with limited in situ data [53,57].

4.3. Relationship Between Topographic Variables

The topographic influences on SWE differ between MTerra and MAqua. In MTerra, SWE showed higher values on gentle slopes and on west-facing slopes (Table 5). The maximum SWE was on slopes between 4° and 14°; by contrast, according to [57], the maximum SCA was on slopes between 20° and 30° in the western Himalayas, but Kour et al. [58] found that the maximum SCA was found on slopes of 5–10°, while Chu et al. [59]

found the maximum SCA in 5–10° slopes and a strong influence of elevation, similar to our results, which found the highest SWE on slopes less than 10° (Figure 4b,e).

In contrast to MTerra, SWE results derived from MAqua did not show a significant relationship with any of the analyzed topographic variables. However, in some regions, such as China, previous studies have reported that higher elevation is associated with faster snowmelt [24]. Other studies have also found that elevation strongly influenced the variability of snow accumulation, mainly due to temperature gradients and the timing of storm events [23,51,58].

In forested and shrubland areas, aspect has been reported to be a controlling factor in snow depth variability [60], with high variability of snowpack variability in north faces [61]. In the Sierra Nevada, California, the deepest snowpack was found on NW-facing slopes [60]. In the SSPM, we found that the highest SWE was in the SW-facing (MTerra) and NW-facing slopes (MAqua), but the lowest was in the NE-facing slopes for both satellites (MTerra and MAqua). Other studies found a greater SCA on north-facing slopes [57,59,62] or on south- and east-facing slopes [56,61]. It is also possible that vegetation density differs subtly between west- and east-facing slopes, influencing snow retention through shading and interception effects. Detailed canopy structure analysis would be needed to test this hypothesis. Broxton et al. [63] found that lower vegetation cover reduces the SWE on south-facing slopes because shadows from vegetation reduce the melt flux, and in dense forest, the SWE is lower than in sparse forest due to canopy interception [64].

5. Conclusions

We analyzed the interannual variability of SCA and SWE of ephemeral snow and its distribution based on topographic variables in the SSPM forest. Local optimal thresholds of NDSI were determined by varying NDSI thresholds from 0 to 100 and creating binary SCA maps for each threshold. For the open forest in SSPM, we found thresholds of 6.4 (MTerra) and 5.3 for MAqua, which is consistent with other locations with forest cover and/or thin snowpacks.

Annual maximum values of SWE ranged from 14 mm to 190 mm, averaging about 55 mm in dry water years (DWY) and 91 mm in wet water years. The months with the highest SWE values were March (MTerra) and February (MAqua). SWE was slightly overestimated by MAqua (mean bias = 0.05 mm) and slightly underestimated by MTerra (-0.06 mm), while the matched dataset showed a bias of -0.02 mm, reflecting sensitivity to satellite overpass timing. Although overall accuracy in estimating SCA and SWE was good, MODIS V6 sensitivity remains limited in ephemeral snow in low-density forests; snowfall events were identified by combining NDSI-derived SCA with temperature (≤ 4 °C) and precipitation data from ERA5-Land to reduce false detections under marginal thermal conditions.

We conclude that mapping SCA and SWE in dynamic ephemeral snow conditions must take into account differences in overpass times of the satellite (MTerra or MAqua), combined with the topographic characteristics and environmental variables. For SWE derived from MTerra, aspect (Eastness) emerged as the only statistically significant topographic control in the regression analysis, while slope and elevation showed non-significant tendencies. The stronger topographic control observed in MTerra may be related to the closer alignment between Terra overpass timing and morning field measurements, as well as reduced melt effects earlier in the day.

For future investigations of snow cover and its snow water equivalent, it is essential to augment the dataset of in situ measurements of snow depth and to increase the number of camera traps along the SSPM, but preferably in other vegetation types and across different topographic variables such as elevation, slope, and facing aspects, to improve the SWE

estimates. It will be important to use different sources of information and methods like machine learning and other emerging techniques in remote sensing (such as LiDAR, UAV (Unmanned Aerial Vehicle) mapping, or GNSS-IR) to capture ephemeral snow dynamics. Citizen science will be an important strategy to estimate ephemeral snow variables (snow depth, snow phenology, or snow cover) through the involvement of the population that visits the SSPM during the winter.

Finally, this work provides valuable information on SCA and the SWE in a location where the field data is scarce to improve conservation strategies, management strategies, and regulation of water resources in Mexican Mediterranean mountain areas with ephemeral snow cover.

Author Contributions: Conceptualization, M.E.E.-B., T.W.B. and N.G.-E.; methodology, M.E.E.-B. and T.W.B.; software, N.G.-E.; validation, M.E.E.-B. and T.W.B.; formal analysis, M.E.E.-B.; investigation, M.E.E.-B.; data curation, M.E.E.-B.; writing—original draft preparation, M.E.E.-B., T.W.B. and N.G.-E.; writing—review and editing, M.E.E.-B., T.W.B., N.G.-E., A.G.-O., G.R.-C. and L.G.M.-E.; visualization, M.E.E.-B.; supervision, T.W.B., N.G.-E. and A.G.-O. All authors have read and agreed to the published version of the manuscript.

Funding: This research received no external funding.

Data Availability Statement: Daily MODIS snow products (Terra and Aqua) and ERA 5 Land-hourly used during the current study are publicly available in the catalog of GEE (Earth Engine Data Catalog | Google for Developers (https://developers.google.com/earth-engine/datasets/) accessed on 8 February 2026). The GEE codes developed in this study are available from the corresponding author on reasonable request.

Acknowledgments: The author [M.E.E.-B.] acknowledges the financial support provided by the Secretaría de Ciencia, Humanidades, Tecnología e Innovación (SECIHTY), México, through a doctoral scholarship. The author [M.E.E.-B.] also acknowledges the Laboratorio de Oceanografía aérea del IIO-UABC for software licensing (ArcGIS Pro, version 3.2.0). The authors are grateful to the administration and personnel of Sierra de San Pedro Mártir Natural Park for providing field support. Also, the authors are grateful to Aldo Guevara-Carrizales from Facultad de Ciencias—UABC for providing the images of the camera traps used for the validation. The authors would like to thank the reviewers for their valuable suggestions.

Conflicts of Interest: The authors declare no conflicts of interest.

Abbreviations

The following abbreviations are used in this manuscript:

SWE	Snow water equivalent
ES	Ephemeral snow
MODIS	Moderate-Resolution Imaging Spectroradiometer
SSPM	Sierra de San Pedro Mártir
SCA	Snow cover area
NDSI	Normalized difference snow index
GEE	Google Earth Engine
ROC	Receiver-Operating-Characteristic
SPEI	Standardized Precipitation Evapotranspiration Index
DWY	Dry water year
WWY	Wet water year
NWY	Normal water year
RMSE	Root mean square error
NRMSE	Normalized root mean square error

Appendix A

Appendix A.1

We use a confusion matrix to determine the optimal local threshold for ephemeral snow using MODIS observations and images for a camera traps.

Table A1. Confusion matrix between MODIS observations and camera trap observations in the SSPM.

	Predicted Classes (MODIS)	
Actual classes (camera traps images)	Snow	No snow
Snow	TP [1]	FN [2]
No snow	FP [3]	TN [4]

[1] TP: true positive (actual and predicted class were snow); [2] FN: false negative (actual was snow and predicted class was no snow); [3] FP: false positive (actual was no snow and predicted class were snow); [4] TN: true negative (actual and predicted class were no snow).

To assess the performance of the binary classification we determine, the following equations were used for each metric:

$$\text{OA} = \frac{TP + TN}{TP + TN + FP + FN}, \quad \text{(A1)}$$

$$P = \frac{TP}{TP + FP}, \quad \text{(A2)}$$

$$\text{SP} = \frac{TN}{TN + FP}, \quad \text{(A3)}$$

$$S = \frac{TP}{TP + FN}, \quad \text{(A4)}$$

where *TP* is true positive, *TN* is true negative, *FP* is false positive, and *FN* is false negative. Overall accuracy (OA) is the percentage of observations that are correctly classified; the precision (P) is the ratio of the correct positives to the total number of positive observations; specificity (SP) is the ratio of correct negatives to all negative classes in the classification (Equation (A3)); and sensitivity (S) is the ratio of correct positives to all positives in the classification (Equation (A4)).

The camera trap images capture the depletion of snowpack between the passage of the MTerra and MAqua satellites (Figure A1).

Figure A1. Example of one image taken from the camera trap in the SSPM: (**a**) morning image and (**b**) evening image in an observed snowfall event.

Appendix A.2

In addition to the clear differences between SCA and its SWE during satellite overpasses, these differences become more evident under varying climatic conditions (wet, normal, and dry years) (Figure A2).

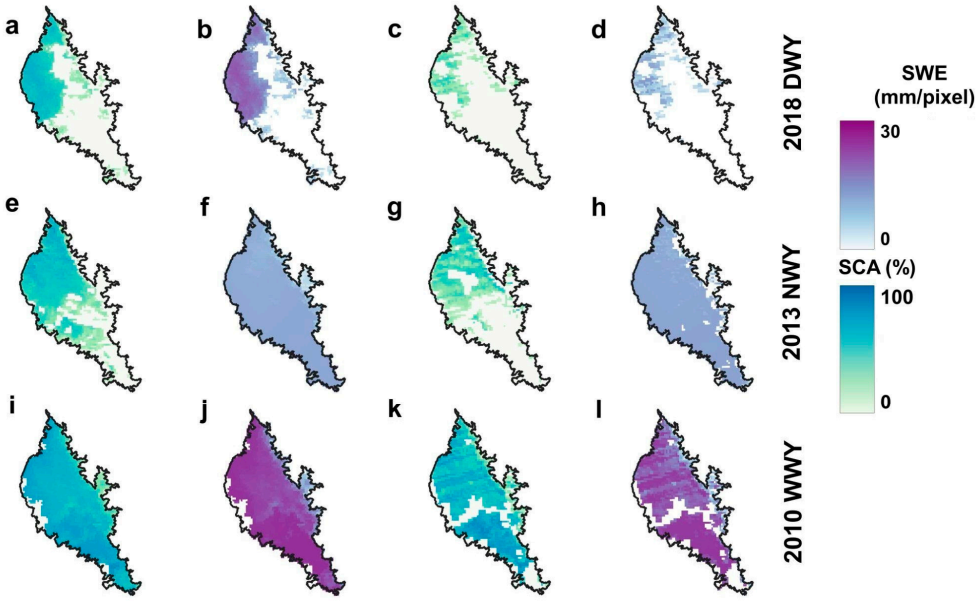

Figure A2. Spatial distribution of SCA and SWE from MTerra (**a**,**b**,**e**,**f**,**i**,**j**) and MAqua (**c**,**d**,**g**,**h**,**k**,**l**) observations for a day with the highest values of SCA and SWE estimation in three different years.

References

1. Notarnicola, C. Hotspots of Snow Cover Changes in Global Mountain Regions over 2000–2018. *Remote Sens. Environ.* **2020**, *243*, 111781. [CrossRef]
2. Shulgina, T.; Gershunov, A.; Hatchett, B.J.; Guirguis, K.; Subramanian, A.C.; Margulis, S.A.; Fang, Y.; Cayan, D.R.; Pierce, D.W.; Dettinger, M.; et al. Observed and Projected Changes in Snow Accumulation and Snowline in California's Snowy Mountains. *Clim. Dyn.* **2023**, *61*, 4809–4824. [CrossRef]
3. Petersky, R.; Harpold, A. Now You See It, Now You Don't: A Case Study of Ephemeral Snowpacks and Soil Moisture Response in the Great Basin, USA. *Hydrol. Earth Syst. Sci.* **2018**, *22*, 4891–4906. [CrossRef]
4. Siirila-Woodburn, E.R.; Rhoades, A.M.; Hatchett, B.J.; Huning, L.S.; Szinai, J.; Tague, C.; Nico, P.S.; Feldman, D.R.; Jones, A.D.; Collins, W.D.; et al. A Low-to-No Snow Future and Its Impacts on Water Resources in the Western United States. *Nat. Rev. Earth Environ.* **2021**, *2*, 800–819. [CrossRef]
5. Slatyer, R.A.; Umbers, K.D.L.; Arnold, P.A. Ecological Responses to Variation in Seasonal Snow Cover. *Conserv. Biol.* **2022**, *36*, e13727. [CrossRef] [PubMed]
6. López-Moreno, J.I.; Callow, N.; McGowan, H.; Webb, R.; Schwartz, A.; Bilish, S.; Revuelto, J.; Gascoin, S.; Deschamps-Berger, C.; Alonso-González, E. Marginal Snowpacks: The Basis for a Global Definition and Existing Research Needs. *Earth-Sci. Rev.* **2024**, *252*, 104751. [CrossRef]
7. López Moreno, J.I.; Deschamps-Berger, C.; Revuelto, J.; Alonso-GonzÁlez, E.; Rojas-Heredia, F.; Callow, N. The Response of Marginal Snowpacks to Climate Warming. *Adv. Clim. Change Res.* **2025**, *16*, 900–909. [CrossRef]
8. Sturm, M.; Liston, G.E. Revisiting the Global Seasonal Snow Classification: An Updated Dataset for Earth System Applications. *J. Hydrometeorol.* **2021**, *22*, 2917–2938. [CrossRef]
9. Fayad, A.; Gascoin, S.; Faour, G.; López-Moreno, J.I.; Drapeau, L.; Page, M.L.; Escadafal, R. Snow Hydrology in Mediterranean Mountain Regions: A Review. *J. Hydrol.* **2017**, *551*, 374–396. [CrossRef]
10. Dwivedi, R.; Biederman, J.A.; Broxton, P.D.; Lee, K.; van Leeuwen, W.J.D. Snowtography Quantifies Effects of Forest Cover on Net Water Input to Soil at Sites with Ephemeral or Stable Seasonal Snowpack in Arizona, USA. *Ecohydrology* **2023**, *16*, e2494. [CrossRef]
11. Nadal-Romero, E.; López-Moreno, J.I. The Hydrological Response of Melting Ephemeral Snowpacks Compared to Winter Rainfall Events in a Mid-Mountainous Pyrenean Catchment. *Mediterr. Geosci. Rev.* **2025**, *7*, 649–662. [CrossRef]

12. Dwivedi, R.; Biederman, J.A.; Broxton, P.D.; Lee, K.; van Leeuwen, W.J.D.; Pearl, J.K. Forest Density and Snowpack Stability Regulate Root Zone Water Stress and Percolation Differently at Two Sites with Contrasting Ephemeral vs. Stable Seasonal Snowpacks. *J. Hydrol.* **2023**, *624*, 129915. [CrossRef]
13. Wiggins, H.L.; Nelson, C.R.; Larson, A.J.; Safford, H.D. Using LiDAR to Develop High-Resolution Reference Models of Forest Structure and Spatial Pattern. *For. Ecol. Manag.* **2019**, *434*, 318–330. [CrossRef]
14. Hatchett, B.J. Seasonal and Ephemeral Snowpacks of the Conterminous United States. *Hydrology* **2021**, *8*, 32. [CrossRef]
15. Riggs, G.A.; Hall, D.K.; Román, M.O. *MODIS Snow Products Collection 6.1 User Guide*; National Snow and Ice Data Center: Boulder, CO, USA, 2015; Volume 66, p. 545.
16. Bousbaa, M.; Boudhar, A.; Kinnard, C.; Elyoussfi, H.; Karaoui, I.; Eljabiri, Y.; Bouamri, H.; Chehbouni, A. An Accurate Snow Cover Product for the Moroccan Atlas Mountains: Optimization of the MODIS NDSI Index Threshold and Development of Snow Fraction Estimation Models. *Int. J. Appl. Earth Obs. Geoinf.* **2024**, *129*, 103851. [CrossRef]
17. Tong, R.; Parajka, J.; Komma, J.; Blöschl, G. Mapping Snow Cover from Daily Collection 6 MODIS Products over Austria. *J. Hydrol.* **2020**, *590*, 125548. [CrossRef]
18. Zhang, H.; Zhang, F.; Zhang, G.; Che, T.; Yan, W.; Ye, M.; Ma, N. Ground-Based Evaluation of MODIS Snow Cover Product V6 across China: Implications for the Selection of NDSI Threshold. *Sci. Total Environ.* **2019**, *651*, 2712–2726. [CrossRef]
19. Breen, C.; Vuyovich, C.; Odden, J.; Hall, D.; Prugh, L. Evaluating MODIS Snow Products Using an Extensive Wildlife Camera Network. *Remote Sens. Environ.* **2023**, *295*, 113648. [CrossRef]
20. Strickfaden, K.M.; Behan, M.L.; Marshall, A.M.; Svancara, L.K.; Ausband, D.E.; Link, T.E. Virtual Snow Stakes: A New Method for Snow Depth Measurement at Remote Camera Stations. *Wildl. Soc. Bull.* **2023**, *47*, e1481. [CrossRef]
21. Molotch, N.P.; Margulis, S.A. Estimating the Distribution of Snow Water Equivalent Using Remotely Sensed Snow Cover Data and a Spatially Distributed Snowmelt Model: A Multi-Resolution, Multi-Sensor Comparison. *Adv. Water Resour.* **2008**, *31*, 1503–1514. [CrossRef]
22. Molotch, N.P. Reconstructing Snow Water Equivalent in the Rio Grande Headwaters Using Remotely Sensed Snow Cover Data and a Spatially Distributed Snowmelt Model. *Hydrol. Process.* **2009**, *23*, 1076–1089. [CrossRef]
23. Rittger, K.; Bair, E.H.; Kahl, A.; Dozier, J. Spatial Estimates of Snow Water Equivalent from Reconstruction. *Adv. Water Resour.* **2016**, *94*, 345–363. [CrossRef]
24. Liu, M.; Xiong, C.; Pan, J.; Wang, T.; Shi, J.; Wang, N. High-Resolution Reconstruction of the Maximum Snow Water Equivalent Based on Remote Sensing Data in a Mountainous Area. *Remote Sens.* **2020**, *12*, 460. [CrossRef]
25. Plauchu-Frayn, I.; Colorado, E.; Richer, M.G.; Herrera-Vázquez, C.; Plauchu-Frayn, I.; Colorado, E.; Richer, M.G.; Herrera-Vázquez, C. Thirteen Years of Weather Statistics at San Pedro Mártir Observatory. *Rev. Mex. Astron. Astrofís* **2020**, *56*, 295–319. [CrossRef]
26. Higgins, R.W.; Yao, Y.; Wang, X.L. Influence of the North American Monsoon System on the U.S. Summer Precipitation Regime. *J. Clim.* **1997**, *10*, 2600–2622. [CrossRef]
27. Minnich, R.A.; Barbour, M.G.; Burk, J.H.; Sosa-Ramírez, J. Californian Mixed-Conifer Forests under Unmanaged Fire Regimes in the Sierra San Pedro Mártir, Baja California, Mexico. *J. Biogeogr.* **2000**, *27*, 105–129. [CrossRef]
28. Delgadillo, J.; Rodríguez, J.D. *El Bosque de Coníferas de la Sierra de San Pedro Mártir, Baja California*; Instituto Nacional de Ecología: Ciudad de México, Mexico, 2004.
29. Thorne, R.; Moran, R.; Minnich, R. Vascular Plants of the High Sierra San Pedro Mártir, Baja California, Mexico: An Annotated Checklist. *Aliso J. Syst. Florist. Bot.* **2010**, *28*, 1–50. [CrossRef]
30. Peralta-García, A.; Valdez-Villavicencio, J.H.; Fucsko, L.A.; Hollingsworth, B.D.; Johnson, J.D.; Mata-Silva, V.; Rocha, A.; DeSantis, D.L.; Porras, L.W.; Wilson, L.D. The Herpetofauna of the Baja California Peninsula and Its Adjacent Islands, Mexico: Composition, Distribution, and Conservation Status. *Amphib. Reptile Conserv.* **2023**, *17*, 57–142.
31. Guevara-Carrizales, A.A.; Ruiz-Campos, G.; Escobar-Flores, J.; Martínez-Gallardo, R. Mamíferos de Baja California. Mamíferos terrestres de las ecorregiones áridas del estado de Baja California. In *Riqueza y Conservación de los Mamíferos en México a Nivel Estatal*; Briones-Salas, M., Hortelano-Moncada, Y., Magaña-Cota, G., Sánchez-Rojas, G., Sosa-Escalante, J.E., Eds.; Universidad de Guanajuato: Guanajuato, México, 2016; pp. 63–90.
32. Ruiz-Campos, G.; Contreras Balderas, A.J.; De Leon Giron, G. *Guía de Campo de las Aves de la Sierra de San Pedro Mártir, Baja California*, 1st ed.; Quintanilla Ediciones: Saltillo, México, 2025; ISBN 978-607-8801-59-6.
33. Ruiz-Campos, G.; García De León, F.J. *Peces Continentales de Baja California*; Universidad Autónoma de Baja California: Mexicali, Mexico, 2024.
34. Peinado, M.; Bartolome, C.; Delgadillo, J.; Aguado, I. Pisos de Vegetación de La Sierra de San Pedro Mártir, Baja California, México. *Acta Bot. Mex.* **1994**, *29*, 1–30. [CrossRef]
35. Diario Oficial de la Federación. Decreto por el que se declara Parque Nacional a las montañas que forman la Sierra de San Pedro Mártir, en Ensenada, Distrito Norte de la Baja California y que se destinarán a la conservación perenne de la flora y fauna comarcanas. *Diario Oficial de la Federación*, 26 April 1947, p. 4. Available online: https://www.dof.gob.mx/nota_to_imagen_fs.php?codnota=4643112&fecha=26/04/1947&cod_diario=199831 (accessed on 10 October 2025).

36. Zavala-Alvarez, J.; Valenzuela-Solano, C.; Zavala-Alvarez, J.-C. San Pedro Mártir. Servicios ecosistémicos, beneficiarios y regionalización. *Rev. Latinoam. Recursos Nat.* **2019**, *15*, 35–48.
37. Perilla, G.A.; Mas, J.-F.; Perilla, G.A.; Mas, J.-F. Google Earth Engine (GEE): Una poderosa herramienta que vincula el potencial de los datos masivos y la eficacia del procesamiento en la nube. *Investig. Geográficas* **2020**, *101*, e59929. [CrossRef]
38. Li, S.; Wan, H.; Yu, Q.; Wang, X. Downscaling of ERA5 reanalysis land surface temperature based on attention mechanism and Google Earth Engine. *Sci. Rep.* **2025**, *15*, 675. [CrossRef]
39. Hall, D.K.; Riggs, G.A.; Salomonson, V.V.; DiGirolamo, N.E.; Bayr, K.J. MODIS Snow-Cover Products. *Remote Sens. Environ.* **2002**, *83*, 181–194. [CrossRef]
40. R Core Team. *R: The R Project for Statistical Computing*; R Foundation for Statistical Computing: Vienna, Austria, 2025. Available online: https://www.r-project.org/ (accessed on 29 December 2025).
41. Robin, X.; Turck, N.; Hainard, A.; Tiberti, N.; Lisacek, F.; Sanchez, J.-C.; Müller, M. pROC: An Open-Source Package for R and S+ to Analyze and Compare ROC Curves. *BMC Bioinform.* **2011**, *12*, 77. [CrossRef] [PubMed]
42. Nahm, F.S. Receiver Operating Characteristic Curve: Overview and Practical Use for Clinicians. *Korean J. Anesthesiol.* **2022**, *75*, 25–36. [CrossRef] [PubMed]
43. Dai, A. Temperature and Pressure Dependence of the Rain-Snow Phase Transition over Land and Ocean. *Geophys. Res. Lett.* **2008**, *35*, L12802. [CrossRef]
44. Martinec, J.; Rango, A.; Major, E. The Snowmelt-Runoff Model (SRM) User's Manual. 1983. Available online: https://ntrs.nasa.gov/citations/19830015389 (accessed on 2 January 2026).
45. Vicente-Serrano, S.M.; Beguería, S.; López-Moreno, J.I. A Multiscalar Drought Index Sensitive to Global Warming: The Standardized Precipitation Evapotranspiration Index. *J. Clim.* **2010**, *23*, 1696–1718. [CrossRef]
46. Wang, Q.; Zeng, J.; Qi, J.; Zhang, X.; Zeng, Y.; Shui, W.; Xu, Z.; Zhang, R.; Wu, X.; Cong, J. A Multi-Scale Daily SPEI Dataset for Drought Characterization at Observation Stations over Mainland China from 1961 to 2018. *Earth Syst. Sci. Data* **2021**, *13*, 331–341. [CrossRef]
47. Alpaydin, E. *Introduction to Machine Learning*, 4th ed.; MIT Press: Cambridge, MA, USA, 2020.
48. Nti, I.K.; Nyarko-Boateng, O.; Aning, J. Performance of Machine Learning Algorithms with Different K Values in K-Fold CrossValidation. *Int. J. Inf. Technol. Comput. Sci.* **2021**, *13*, 61–71. [CrossRef]
49. Shao, D.; Li, H.; Wang, J.; Hao, X.; Che, T.; Ji, W. Reconstruction of a Daily Gridded Snow Water Equivalent Product for the Land Region above 45° N Based on a Ridge Regression Machine Learning Approach. *Earth Syst. Sci. Data* **2022**, *14*, 795–809. [CrossRef]
50. Keuris, L.; Hetzenecker, M.; Nagler, T.; Mölg, N.; Schwaizer, G. An Adaptive Method for the Estimation of Snow Covered Fraction with Error Propagation for Applications from Local to Global Scales. *Remote Sens.* **2023**, *15*, 1231. [CrossRef]
51. Yang, Z.; Chen, R.; Liu, Z.; Zhang, W. Estimating Snow Water Equivalent Using Observed Snow Depth Data in China. *J. Hydrol. Reg. Stud.* **2024**, *51*, 101664. [CrossRef]
52. Sankey, T.; Donald, J.; McVay, J.; Ashley, M.; O'Donnell, F.; Lopez, S.M.; Springer, A. Multi-Scale Analysis of Snow Dynamics at the Southern Margin of the North American Continental Snow Distribution. *Remote Sens. Environ.* **2015**, *169*, 307–319. [CrossRef]
53. Akyurek, Z.; Kuter, S.; Karaman, Ç.H.; Akpınar, B. Understanding the Snow Cover Climatology over Turkey from ERA5-Land Reanalysis Data and MODIS Snow Cover Frequency Product. *Geosciences* **2023**, *13*, 311. [CrossRef]
54. Da Ronco, P.; Avanzi, F.; De Michele, C.; Notarnicola, C.; Schaefli, B. Comparing MODIS Snow Products Collection 5 with Collection 6 over Italian Central Apennines. *Int. J. Remote Sens.* **2020**, *41*, 4174–4205. [CrossRef]
55. Riggs, G.A.; Hall, D.K.; Román, M.O. Overview of NASA's MODIS and Visible Infrared Imaging Radiometer Suite (VIIRS) Snow-Cover Earth System Data Records. *Earth Syst. Sci. Data* **2017**, *9*, 765–777. [CrossRef]
56. Parajka, J.; Holko, L.; Kostka, Z.; Blöschl, G. MODIS Snow Cover Mapping Accuracy in a Small Mountain Catch ment—Comparison between Open and Forest Sites. *Hydrol. Earth Syst. Sci.* **2012**, *16*, 2365–2377. [CrossRef]
57. Sahu, R.; Gupta, R.D. Snow Cover Area Analysis and Its Relation with Climate Variability in Chandra Basin, West ern Himalaya, during 2001–2017 Using MODIS and ERA5 Data. *Environ. Monit. Assess.* **2020**, *192*, 489. [CrossRef]
58. Kour, R.; Patel, N.; Krishna, A.P. Effects of Terrain Attributes on Snow-Cover Dynamics in Parts of Chenab Basin, Western Himalayas. *Hydrol. Sci. J.* **2016**, *61*, 1861–1876. [CrossRef]
59. Chu, D.; Liu, L.; Wang, Z. Snow Cover on the Tibetan Plateau and Topographic Controls. *Remote Sens.* **2023**, *15*, 4044. [CrossRef]
60. Kirchner, P.B.; Bales, R.C.; Molotch, N.P.; Flanagan, J.; Guo, Q. LiDAR Measurement of Seasonal Snow Accumu lation along an Elevation Gradient in the Southern Sierra Nevada, California. *Hydrol. Earth Syst. Sci.* **2014**, *18*, 4261–4275. [CrossRef]
61. Tennant, C.J.; Harpold, A.A.; Lohse, K.A.; Godsey, S.E.; Crosby, B.T.; Larsen, L.G.; Brooks, P.D.; Van Kirk, R.W.; Glenn, N.F. Regional Sensitivities of Seasonal Snowpack to Elevation, Aspect, and Vegetation Cover in Western North America. *Water Resour. Res.* **2017**, *53*, 6908–6926. [CrossRef]
62. Safa, H.; Krogh, S.A.; Greenberg, J.; Kostadinov, T.S.; Harpold, A.A. Unraveling the Controls on Snow Disappear ance in Montane Conifer Forests Using Multi-Site Lidar. *Water Resour. Res.* **2021**, *57*, e2020WR027522. [CrossRef]

63. Banerjee, A.; Chen, R.; Meadows, M.E.; Sengupta, D.; Pathak, S.; Xia, Z.; Mal, S. Tracking 21st Century Climate Dynamics of the Third Pole: An Analysis of Topo-Climate Impacts on Snow Cover in the Central Himalaya Using Google Earth Engine. *Int. J. Appl. Earth Obs. Geoinf.* **2021**, *103*, 102490. [CrossRef]
64. Broxton, P.D.; van Leeuwen, W.J.D.; Biederman, J.A. Forest Cover and Topography Regulate the Thin, Ephemeral Snowpacks of the Semiarid Southwest United States. *Ecohydrology* **2020**, *13*, e2202. [CrossRef]